Acta Cryst. (1995). A51, 375–384

Properties of Grazing-Angle X-ray Standing Waves and their Application to an Arsenic-Deposited Si (111) 1×1 Surface

BY O. SAKATA* AND H. HASHIZUME

Research Laboratory of Engineering Materials, Tokyo Institute of Technology, Nagatsuta, Midori, Yokohama 226, Japan

(*Received* 24 *August* 1994; *accepted* 25 *November* 1994)

Abstract

Grazing-angle diffraction of X-rays by crystal planes normal to a surface generates dynamical (lattice-modulated) standing waves, which are used in this paper to determine the in-plane structure of arsenic adatoms on an Si (111) surface of the 1×1 structure. The X-ray field, formed by the interference of the incident, specular-reflected and Bragg-diffracted beams above the surface, has two components with and without intensity modulation in the direction of the reciprocal-lattice vector parallel to the surface. The two components behave differently as a function of X-ray glancing incidence angle on the surface in the vicinity of the critical angle for total external reflection. This property has been exploited to determine the ordering of the As atoms accurately using X-ray fluorescence signals observed from a sample in ultra-high vacuum at a synchrotron source. The data show highly ordered As atoms occupying the threefold-coordinated sites on the bulk-like Si (111) surface. Displaced arsenic positions are not supported by the observation. The conclusion is fairly insensitive to the vertical height of the overlayer atoms used in the analysis, in accordance with the slow variation of the field profile along the surface normal. The grazing-angle X-ray standing-wave method allows model-independent determination of the registry of foreign atoms at a crystal surface with a positional accuracy of a few hundredths of an Å.

1. Introduction

Grazing-angle X-ray diffraction has gained a wide popularity in surface structure determination (Robinson, 1991). Bragg reflections, which emerge out of a surface for small glancing-incidence angles of X-rays close to the critical angle for total external reflection, are measured here from two-dimensional arrays of atoms. The X-ray field penetrates into shallow layers lying inside the surface of a substrate crystal under a specular-reflection condition. Cowan (1985) demonstrated that diffraction of evanescent X-rays in such a layer generates dynamical (lattice-modulated) standing waves and that these waves are useful for determination of the in-plane structure of foreign atoms at surfaces and interfaces by monitoring secondary emissions. The reciprocal-lattice vector is here directed nearly parallel to the surface, unlike the conventional Bragg standing-wave experiments using out-of-surface reciprocal-lattice vectors. The geometry is classified in the Laue case of diffraction but, unlike the usual ones in the absence of a specular reflection, zero, one and two Bloch waves are produced in the crystal depending on the X-ray incidence angles (Cowan, 1985; Sakata & Hashizume, 1987). This predominates over the nature of the external field, which is more complicated than in the Bragg geometry, involving incident, specular-reflected and Bragg diffracted beams outside the surface. At certain incidence angles, the vacuum diffracted wave becomes evanescent, hence the standing-wave field is confined in a thin layer immediately above the surface. Standing-wave effects were first observed in the X-ray fluorescence (Cowan, Brennan, Jach, Bedzyk & Materlik, 1986; Hashizume & Sakata, 1989*a*) and electron emissions (Afanasev, Imamov, Maslov & Mukhamedzhanov, 1989) from lattice atoms of bulk crystals. The technique was then applied to the registration of iodine adatoms with respect to Ge (111) surface atoms in the open-air environment (Jach & Bedzyk, 1990).

We reported a first observation of fluorescence signals from arsenic adatoms on an Si (111) surface, modulated by a grazing-angle standing-wave field in ultra-high vacuum (Sakata, Hashizume & Kurashina, 1993). The structure and electronic properties of an arsenic-adsorbed Si (111) surface have been the object of a large body of work. The topics interested surface scientists partly because arsenic deposition removes the complex 7 × 7 reconstruction of the clean Si (111) surface to yield a bulk-like 1 × 1 surface, and partly because As makes the silicon surface passive to produce a chemically stable surface. Our grazing-angle standing-wave data were consistent with the model indicating the As atoms in the threefold-coordinated substitutional sites on the 1 × 1 surface.

We first discuss in §2 the properties of grazing-angle standing waves outside the surface, which have direct relevance to the determination of overlayer structures.

* Author to whom all correspondence should be addressed.

We will show that the field strength can be written as a sum of two terms, position independent and position dependent. The former profile changes sensitively with X-ray glancing-incidence angle on the surface, while the latter profile is markedly different for different lattice positions but each profile only weakly depends on glancing-incidence angle. An examination of the two profiles reveals appropriate glancing-incidence angles to be used in practical experiments. In §3, we describe an experiment for determination of the in-plane structure of arsenic adatoms on the Si (111) 1×1 surface, where ultra-high-vacuum X-ray facilities designed for the purpose will be described. We analyze the data in §4 and determine the lattice position and order parameter for As atoms. §5 concludes the paper with remarks on application of the technique to thin films.

2. Wave-field profile above a crystal surface and emission yield from overlayer atoms

Fig. 1 shows a typical geometry for grazing-angle standing-wave experiments. An X-ray wave $\mathbf{K}_0$ is incident on a flat crystal surface at glancing angle φ_0 and satisfies the Bragg condition on a set of lattice planes perpendicular to the surface ($\theta \simeq \theta_B$). When φ_0 is close to the critical angle for total external reflection, φ_c, a specular wave $\mathbf{K}_s$ and a reflected-diffracted wave $\mathbf{K}_h$ emerge from the surface at grazing take-off angles φ_0 and φ_h, respectively. We assume for $\mathbf{K}_0$ a linearly polarized wave with an $\mathbf{E}$ vector normal to the plane of diffraction. The three coherent waves, $\mathbf{K}_0$, $\mathbf{K}_s$ and $\mathbf{K}_h$, form a stationary field outside the surface, which is intensity modulated in the direction of the reciprocal-lattice vector parallel to the surface. The field is also modulated in the perpendicular direction by wave-vector transfers $(\mathbf{K}_{hz} - \mathbf{K}_{0z})$ and $(\mathbf{K}_{sz} - \mathbf{K}_{0z})$ but these are long-wavelength modulations. The local field intensity at vertical height Z from the surface can be written as

$$A + B(x), \tag{1}$$

where x is the normalized position between the active Bragg planes ($0 \le x < 1$). The x axis is defined parallel to the surface and the Bragg planes are located at $x = n$ with $n = 0, \pm 1, \pm 2, \ldots$. A and $B(x)$ represent, respectively, the position-independent and position-dependent components of the field intensity. Using complex amplitudes ε_0, ε_s and ε_h of the $\mathbf{K}_0$, $\mathbf{K}_s$ and $\mathbf{K}_h$ waves, we can write for A and $B(x)$

$$\begin{aligned} A &= |\varepsilon_0 + \varepsilon_s|^2 + |\varepsilon_h|^2 \\ &= |E_0 + E_s \exp(ia)\exp(i4\pi K\varphi_0 Z)|^2 + |\varepsilon_h|^2, \\ B(x) &= 2|\varepsilon_h||E_o + E_s \exp(ia)\exp(i4\pi K\varphi_0 Z)| \\ &\quad \times \sin(-2\pi x + b + c + \delta), \end{aligned} \tag{2}$$

where

$$\varepsilon_h = \begin{cases} E_h \exp(ib) & \text{for real } \varphi_h, \\ E_h \exp(ib)\exp(-2\pi i K\varphi_h Z) & \text{for imaginary } \varphi_h. \end{cases} \tag{3}$$

$B(x)$ arises from cross terms $\varepsilon_0\varepsilon_h$ and $\varepsilon_s\varepsilon_h$ and represents an oscillatory modulation with a repeat period equal to the lattice spacing. E_0, E_s and E_h are the real positive amplitudes of ε_0, ε_s and ε_h, and a and b are the phases of ε_s and ε_h on the surface ($Z = 0$), respectively. We define the positive Z axis directed into the crystal, hence $Z < 0$ in space above the surface. An imaginary φ_h means an evanescent reflected-diffracted wave in (3). φ_h, given by $\varphi_h = (\varphi_0^2 + 2\Delta\theta \sin 2\theta_B)^{1/2}$, becomes imaginary for $\varphi_0^2 < -2\Delta\theta \sin 2\theta_B$, where $\Delta\theta$ is the deviation from the exact Bragg incidence, $\Delta\theta = \theta - \theta_B$, with θ_B being the Bragg angle (Fig. 1). Discussions were extended in the previous papers (Sakata & Hashizume, 1987; Hashizume & Sakata, 1989*a*) to show that zero, one and two Bloch waves are generated in the crystal depending on the $(\varphi_0, \Delta\theta)$ values. For $\varphi_0^2 < -2\Delta\theta \sin 2\theta_B$, no Bloch wave or only Bloch wave 2 with nodes on the Bragg planes (Fig. 1) is produced in a crystal without X-ray absorption depending on the φ_0 value. Parameters c and δ in (2) are given as (Sakata, 1994)

$$c = \begin{cases} 2\pi K(\varphi_0 - \varphi_h)Z & \text{for real } \varphi_h, \\ 2\pi K\varphi_0 Z & \text{for imaginary } \varphi_h, \end{cases} \tag{4}$$

$$\delta = \tan^{-1}\left[\frac{E_0 + E_s\cos(a + 4\pi K\varphi_0 Z)}{E_s \sin(a + 4\pi K\varphi_0 Z)}\right]. \tag{5}$$

Solving the boundary equations at $Z = 0$ for the grazing-angle diffraction, we find amplitudes E_s and E_h and their phases a and b, which include φ_h as a function of φ_0 and

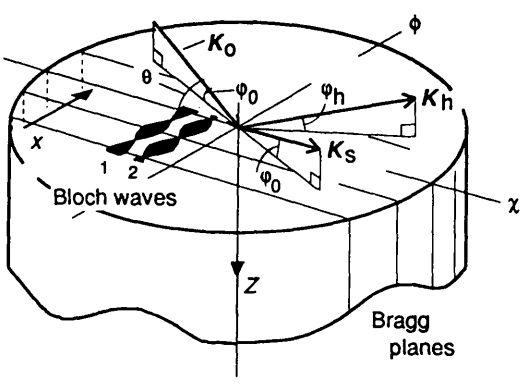

Fig. 1. Geometry for grazing-angle X-ray standing-wave experiments. Incident wave $\mathbf{K}_0$ arrives on a crystal surface at small glancing angle φ_0 making a near Bragg angle θ to the normal Bragg planes. Specular wave $\mathbf{K}_s$ and Bragg-diffracted wave $\mathbf{K}_h$ emerge from the surface at small take-off angles φ_0 and φ_h, respectively. The interference of the $\mathbf{K}_0$, $\mathbf{K}_s$ and $\mathbf{K}_h$ waves generates Bloch waves 1 and 2 having intensity modulations parallel to the surface.

$\Delta\theta$ (Sakata & Hashizume, 1987). Both A and $B(x)$ thus depend on φ_0, $\Delta\theta$ and Z.

Fig. 2 plots A for $Z = 0$ as a function of $\Delta\theta$ for three different values of φ_0 in the case of the 220 reflection of a silicon crystal with 17 keV X-rays. The profile remarkably changes with φ_0 near 1.83 mrad, which is the critical angle φ_c for this case. A peak and a valley are observed in the profile for $\varphi_0 = 1.1$ mrad. This feature can be understood in Fig. 3, where the real and imaginary parts of $[E_0 + E_s \exp(ia)]/E_0$ and $E_h \exp(ib)/E_0$ are plotted in a complex plane. Varying the $\Delta\theta$ value from -50 to 50 μrad drives the phase points in the complex plane on the indicated routes from the square mark in the clockwise direction. A chord connecting a phase point and the origin represents the amplitude of $[E_0 + E_s \exp(ia)]/E_0$ or $E_h \exp(ib)/E_0$ for a particular $\Delta\theta$. The angle that the chord makes to the real axis gives the phase of the relevant quantity. On going from -50 to 50 μrad, phase b of the Bragg diffracted wave decreases by $\sim \pi$ so that the trajectory for $E_h \exp(ib)/E_0$ is not closed, as seen in the inset in Fig. 3.* It is seen that $|[E_0 + E_s \exp(ia)]/E_0|$ peaks at $\Delta\theta \simeq 0$ and then reaches a minimum to come back close to the original value as $\Delta\theta$ increases to 50 μrad. $|E_h \exp(ib)/E_0|$ shows only a peak, and the change in $|E_h \exp(ib)/E_0|$ is a small part of the total change in $|[E_0 + E_s \exp(ia)]/E_0|^2 + |E_h \exp(ib)/E_0|^2$. The profile $A(\Delta\theta)$ is thus dominated by $|[E_0 + E_s \exp(ia)]|^2$. This behavior is correlated with the nature of the internal wave field. For $\varphi_0 < \varphi_c$ under discussion, we have no Bloch wave generated in the crystal in a negative $\Delta\theta$ region and Bloch wave 2 in a positive $\Delta\theta$ region (Sakata & Hashizume, 1987; Hashizume & Sakata, 1989*a*). The peak and the valley in $A(\Delta\theta)$ thus occur at the boundary of the two regions. Similar plots for $\varphi_0 = 1.83$ and 2.6 mrad explain the other profiles shown in Fig. 2.

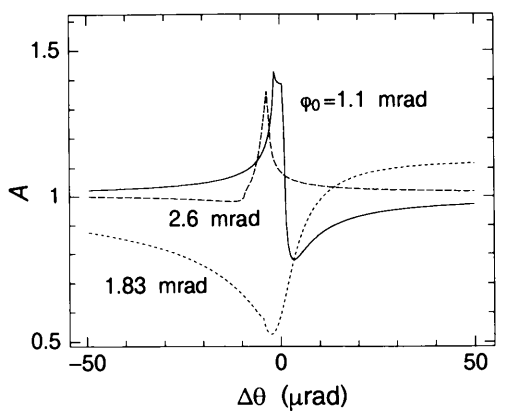

Fig. 2. Profiles of the position-independent term A of the external X-ray field ($Z = 0$) for three values of glancing-incidence angle φ_0. Calculated for the Si 220 reflection with 17 keV X-rays. $\varphi_0 = 1.83$ mrad corresponds to the critical angle for total external reflection.

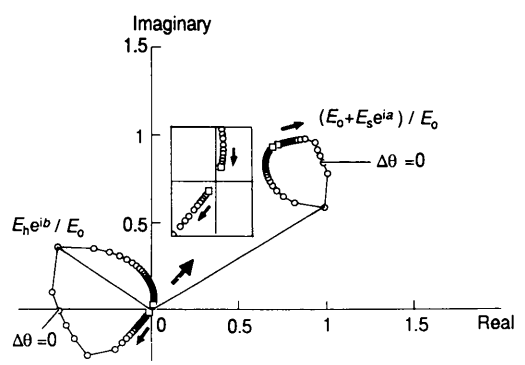

Fig. 3. Wave-amplitude ratios $[E_0 + E_s \exp(ia)]/E_0$ and $E_h \exp(ib)/E_0$ plotted in a complex plane for a change of $\Delta\theta$ from -50 to 50 μrad. Increasing $\Delta\theta$ drives the phase point from and to the square mark on each trajectory in the indicated direction. The inset shows a close-up view of the far Bragg regions for $E_h \exp(ib)/E_0$. Calculated for the Si 220 reflection with 17 keV X-rays at $\varphi_0 = 1.1$ mrad ($Z = 0$).

In (2), position x only appears in the sine function associated with $B(x)$. We have then

$$B(x) = -B(x + 0.5). \tag{6}$$

As to the standing waves generated in the conventional Bragg and Laue geometries, we write $B_B(x)$ and $B_L(x)$ for the position-dependent components of the external field intensities. It can be shown that $B_B(x) = -B_B(x + 0.5)$ for the Bragg case and that $B_L(x) = B_L(1 - x)$ and $B_L(x) = -B_L(x + 0.5)$ for the Laue case. These relations apply to both absorbing and non-absorbing crystals. Formula (6) indicates that grazing-angle standing waves are more similar to the Bragg standing waves, although the former geometry is classified in the Laue geometry where the internal diffracted wave vector is directed into the crystal (Sakata & Hashizume, 1988). Relation (6) can be exploited for structure determination of surface atoms. Fig. 4 plots $B(x)$ *versus* $\Delta\theta$ for $Z = 0$ and $\varphi_0 = \varphi_c$. The very different profiles for $x = 0$, 0.25, 0.5 and 0.75 promise a high sensitivity in atom-position determination from emission data. It can be shown that the $B(x)$ profiles do not show such a drastic change with φ_0 as A even in the vicinity of φ_c (Sakata, 1994).

From (2), the antinodes of the grazing-angle standing waves are located at

$$x_{\text{a.n.}} = [b + c + \delta - (\pi/2)]/2\pi. \tag{7}$$

Fig. 5 plots $x_{\text{a.n.}}$ *versus* $\Delta\theta$ for a few values of φ_0 and $Z = 0$. The functional form of $x_{\text{a.n.}}$ is similar to that for Bragg geometry (Authier, 1986; Saitoh, Hashizume & Tsutsui, 1988) but the underlying mechanisms are not quite the same. In the conventional Bragg geometry, the shift of $x_{\text{a.n.}}$ from near 0.5 to near 0 is caused by the transfer of the wave point from branch 2 [or α in the notation by Batterman & Cole (1964)] to branch 1 (or β)

* A change of $\Delta\theta$ in the range of $-\infty$ to $+\infty$ closes the two trajectories.

of the dynamical dispersion surface as $\Delta\theta$ increases across 0. On the other hand, the wave field in a grazing-angle crystal is a coherent superposition of the two Bloch waves with antinodes fixed on the Bragg planes ($x = 0$) and the middle planes ($x = 0.5$). The node and antinode positions of the total field are determined by the relative excitement of the two Bloch waves. In Fig. 5, $x_{a.n.}$ shifts downwards as φ_0 increases across φ_c (= 1.83 mrad). This is due to a significant decrease in phase b of ε_h.

Fig. 6 plots field intensities A, $B(x)$ and $A + B(x)$ *versus* $\Delta\theta$ at two lateral positions $x = 0$ and 0.5 for $\varphi_0 = 1.1$ and 2.6 mrad, which are located on either side of $\varphi_c = 1.83$ mrad. For the vertical position, we assumed $Z = 0$. For position $x = 0$ (Figs. 6*a* and *b*), profiles of A and $B(x)$ are dissimilar at $\varphi_0 = 1.1$ mrad ($< \varphi_c$), while they are rather similar at $\varphi_0 = 2.6$ mrad ($> \varphi_c$) with peaks at $\Delta\theta \simeq 0$. The situation is reversed for position $x = 0.5$ (Figs. 6*c* and *d*). The excitation probability of fluorescent radiation at an atomic site is proportional to the field intensity at that site. Emission yield from atoms, above the surface, at interplaner position x is proportional to

$$A + fB(x), \tag{8}$$

where f is the fraction of emitting atoms at position x. Other $(1 - f)$ atoms are assumed to occupy random positions. These atoms contribute $(1 - f)A$ to the total emission, while ordered atoms make a contribution of $f\{A + B(x)\}$. The total emission intensity is thus proportional to $(1 - f)A + f\{A + B(x)\} = A + fB(x)$, which is formula (8). We pointed out in the previous paper (Sakata, Hashizume & Kurashina, 1993) that there are appropriate glancing-incidence angles φ_0 to be used in structure studies of surface atoms. For atoms located at $x = 0$, Fig. 6(*a*) shows that profile $A(\Delta\theta) + B(\Delta\theta; x)$ is markedly different from profile $A(\Delta\theta)$ at $\varphi_0 < \varphi_c$, while, in Fig. 6(*b*) for $\varphi_0 > \varphi_c$, they commonly show peaks at $\Delta\theta \simeq 0$. The case is just the opposite for atoms occupying positions $x = 0.5$ (Figs. 6*c* and *d*). If all emissive atoms are ordered in position x ($f = 1$), we would observe an emission profile $A + B(x)$. Disordered structures with all atoms in random positions ($f = 0$) would yield a profile A. Fig. 7 shows how the emission profile varies with f for atoms at $x = 0$. The plotted curves are smeared by the resolution function of a practical experimental set-up: we assumed 10 μrad and 0.2 mrad for spreads in angles θ and φ_0, respectively. Even after the smear, emission profiles for $\varphi_0 < \varphi_c$ show characteristic changes with f value (Fig. 7*a*), whereas at $\varphi_0 > \varphi_c$ (Fig. 7*b*) decreasing f simply reduces a peak-to-valley ratio towards that of A. Glancing angles $\varphi_0 < \varphi_c$ should thus be used in experiments aiming at an accurate determination of the ordering of atoms at $x \simeq 0$. A similar line of discussion favors $\varphi_0 > \varphi_c$ for atoms at $x \simeq 0.5$.

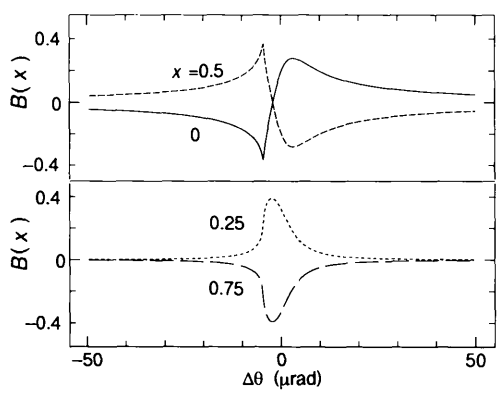

Fig. 4. Profiles of position-dependent term $B(x)$ of the external X-ray field shown for normalized lattice positions $x = 0$, 0.5, 0.25 and 0.75. Calculated for the Si 220 reflection with 17 keV X-rays at $\varphi_0 = 1.83$ mrad ($= \varphi_c$) ($Z = 0$).

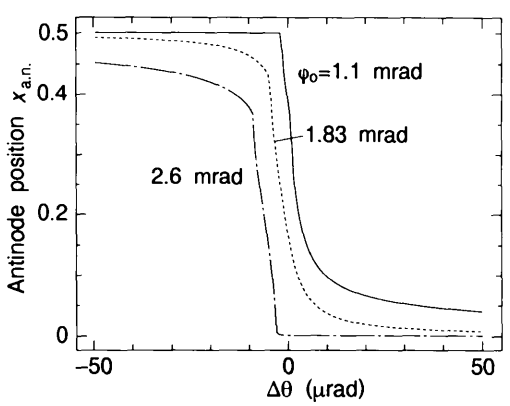

Fig. 5. Antinode positions $x_{a.n.}$ of a grazing-angle standing wave for three glancing-incidence angles φ_0. Bragg planes are located at $x = 0$ and 1.0. Calculated for the Si 220 reflection with 17 keV X-rays ($Z = 0$). $\varphi_0 = 1.83$ mrad corresponds to the critical angle for total external reflection.

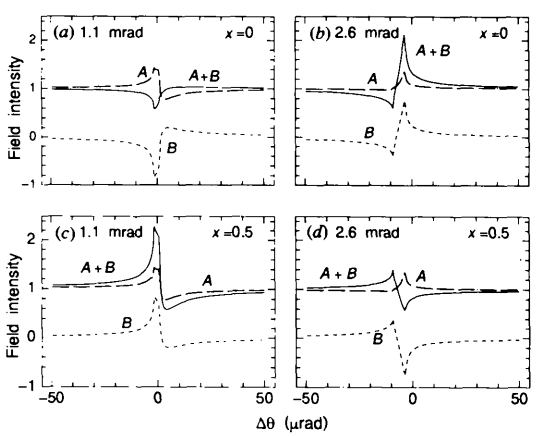

Fig. 6. Profiles of position-independent field A, position-dependent field B and total field intensity $A + B$ of grazing-angle standing waves for normalized lattice positions $x = 0$ [(*a*) and (*b*)] and $x = 0.5$ [(*c*) and (*d*)] on a crystal surface at X-ray glancing-incidence angles 1.1 mrad [(*a*) and (*c*)] and 2.6 mrad [(*b*) and (*d*)]. Calculated for the Si 220 reflection with 17 keV X-rays. $\varphi_c = 1.83$ mrad.

Term A represents an average field intensity: averaging (8) over all x, we have $\langle A + fB(x)\rangle = A$. This term corresponds to (1 + R) in the expression of the conventional Bragg standing-wave field, where R is the reflectivity drawing a familiar rocking-curve profile when plotted *versus* $\Delta\theta$. Both A and (1 + R) involve no information on the position of ordered atoms and describe a background for variable emission profiles with order parameter. While we have a fixed (1 + R) profile for a particular set-up of a Bragg standing-wave experiment, we can enhance the order-parameter sensitivity of a grazing-angle set-up by operating in an appropriate φ_0 range.

Fig. 8 shows a three-dimensional plot of field profile $A(Z) + B(x, Z)$ near the surface ($Z = 0$) for $\varphi_0 = \varphi_c$ and $\Delta\theta < -\varphi_c^2/(2\sin 2\theta_B)$. The field is continuous across the surface, as expected from the boundary conditions imposed in the calculation. The profile shows a modulation by Bloch wave 2 with nodes on the Bragg planes in the x direction. The perpendicular modulation of the external field is largely due to wave-vector transfer ($K_{sz} - K_{0z}$) but its phase is affected by the Bragg diffraction. The field strength on $x = 0$ peaks 12 Å above the surface in Fig. 8. In the absence of the Bragg diffraction, it would have a peak on the surface since the $\mathbf{K}_0$ and $\mathbf{K}_s$ waves are in phase at $\varphi_0 = \varphi_c$ for a medium with negligible X-ray absorption. The vertical peak position depends on x, reflecting the varying phase of the Bragg wave with x. The evanescent $\mathbf{K}_h$ wave exponentially decays with distance from the surface, which is represented by a free-space intensity attenuation coefficient (Sakata & Hashizume, 1987)

$$\mu_h = -4\pi K[-\varphi_0^2 - 2\Delta\theta(\sin 2\theta_B)]^{1/2}. \qquad (9)$$

The negative μ_h conforms to the convention to measure negative Z in the outward direction. $|\mu_h|$ amounts to 0.034 Å^{-1} in the example shown in Fig. 8. The standing-wave modulation in the x direction thus dies out at some distance from the surface. This was termed 'superficial wave' by Cowan *et al.* (1986). In Fig. 8, the field is almost flat in the x direction $\sim$ 100 Å above the surface. The internal field penetrates into the crystal to a depth of the same order of magnitude at φ_0 less than φ_c because of extinction effects. The X-ray fields are thus localized in shallow layers lying both just outside and inside the surface in this range of (φ_0,$\Delta\theta$) angles. It is an interesting issue to see how this is affected by microroughness of the boundary surface.

3. Experimental

Rectangular substrates with tapered side surfaces were tailored from accurately oriented Si (111) plates. The upper surfaces of the substrates, 14 × 19 mm in area, were mechanochemically polished with a standard technique to a flatness of three fringes over more than 90% of the area under a Fiseau interferometer using 5876 Å light. The final substrate thickness was 2.2 mm. The polished surface was chemically cleaned by the use of the Shiraki etch procedure (Ishizaka & Shiraki, 1986). The substrate, mounted on a molybdenum holder, was introduced into a molecular-beam-epitaxy facility (2×10^{-8} Pa) and radiatively heated to 1073 K. A sharp 7 × 7 RHEED (reflection high-energy electron diffraction) pattern was produced in 3 h. We used the moderate annealing temperature to minimize the growth of silicon

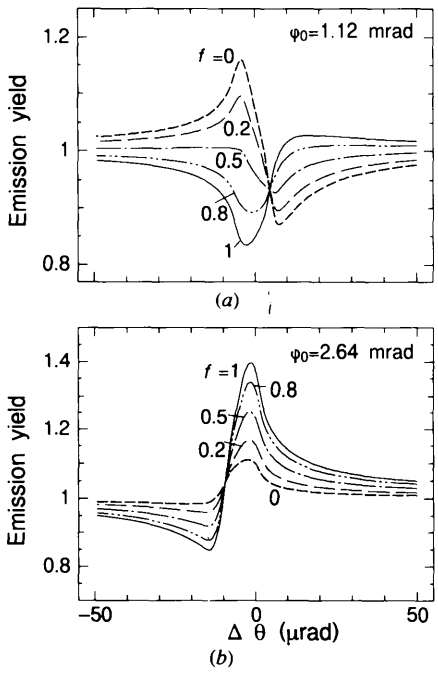

Fig. 7. Variation of emission profile from atoms ordered on the Bragg planes with coherent fraction f. Calculated for the Si 220 reflection with 17 keV X-rays (φ_c = 1.83 mrad). The X-ray glancing-incidence angle φ_0 is 1.12 mrad for (*a*) and 2.64 mrad for (*b*). Smeared by a resolution function of a practical experimental setup.

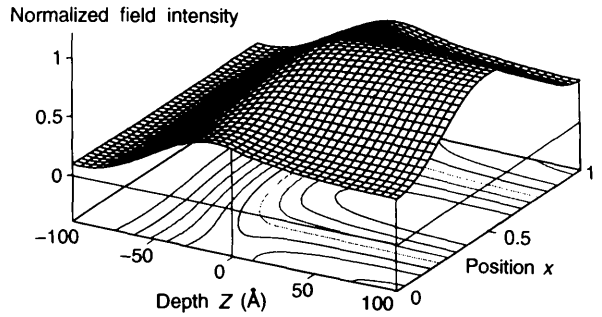

Fig. 8 Two-dimensional profile of X-ray field intensity near the surface of a silicon crystal in grazing-angle diffraction for the ($\bar{2}20$) planes perpendicular to the surface. The surface is located at $Z = 0$ and the crystal occupies space $Z > 0$. The Bragg planes are located at $x = 0$ and 1.0. Calculated for φ_0 = 1.83 mrad and $\Delta\theta = -10.0$ μrad with 17 keV photons.

carbide, which could degrade the ordering of As atoms. Arsenic was deposited on the clean silicon surface from an outgassed effusion cell operated at 523–573 K. The sample was then cooled to 673 K in 30 min before the As-beam shutter was closed. The pressure at the sample position during this time was 6×10^{-5} Pa. This procedure is essentially the same as that employed by other authors to obtain a near-monolayer coverage of Si(111) by As (Patel, Golovchenko, Freeland & Gossmann, 1987; Headrick & Graham, 1988). Sharp 1×1 RHEED spots were observed from the sample at room temperature. The pattern was not, however, free from weak streaks ascribable to silicon carbide.

The prepared Si(111):As 1×1 sample was taken into a portable vacuum vessel, which was transported to a synchrotron-radiation site for X-ray experiments. A small sputter-ion pump ($8\,l\,s^{-1}$ for N_2), powered by a car battery, maintained vacuum in the vessel at less than 2×10^{-6} Pa during the transportation. The sample was transferred into an ultra-high-vacuum (UHV) X-ray scattering chamber *via* a loadlock system at the synchrotron site (Sakata & Hashizume, 1995). Fig. 9 shows the UHV X-ray facility designed for the present experiment. The chamber, 146 mm in inner diameter and 380 mm in height, is evacuated to a pressure of 4×10^{-7} Pa with a $16\,l\,s^{-1}$ sputter-ion pump and a $100\,l\,s^{-1}$ titanium getter pump. At the top of the chamber is mounted a sample-introduction port, which mates the 114 mm Conflat flange of the transportation vessel. Inside the chamber, the sample is held in a horizontal position, with the As-deposited surface upward, on a molybdenum holder bayoneted into a receptacle associated with a rotary-motion feedthrough. The feedthrough, supported on in-air crossed swivels *via* flexible bellows, allowed us to control the azimuthal rotation of an in-vacuum sample around the ω axis shown in Fig. 1. This motion was used to bring the Si $(\bar{2}20)$ planes to the Bragg position. Swivel motions controlled the sample inclination around the horizontal φ and χ axes (Fig. 1). The chamber is equipped with three beryllium windows, 0.2 and 0.4 mm thick, for incoming and outgoing (specular, diffracted and fluorescent) X-rays (inset in Fig. 9). A re-entrant design of the fluorescence window allowed an energy-dispersive detector to have a short access to the sample surface (45 mm). The whole assembly, weighing about 85 kg, sits on the vertical axis of a high-precision rotary table (Nakayama *et al.*, 1986), which is driven when a $\Delta\theta$ scan is performed.

Experiments were carried out on beamline 14B at the Photon Factory synchrotron source in KEK, Tsukuba, Japan. This line delivers vertically polarized synchrotron light from a 5 T superconducting vertical wiggler (Fig. 10). The set-up is similar to those used in the previous grazing-angle diffraction experiments (Sakata & Hashizume, 1988; Hashizume & Sakata, 1989*b*), but here the sample was placed in the UHV chamber. Photons of 16.84 keV energy were extracted by a slightly detuned double-silicon (111) pre-monochromator, which rejected higher harmonic components. The X-ray beam was horizontally reflected by the (220) planes in a silicon symmetric monochromator and passed through a 0.13 (V) $\times$ 1.0 mm (H) slit onto the sample in the UHV chamber. It made a small glancing angle to the sample surface and a near Bragg angle ($\sim$11.05°) to the $(\bar{2}20)$ planes, arranged in a nondispersive position with respect to the monochromator (220) planes. The plane of diffraction was thus horizontal in the present experiment. The technique used to align the crystal was the same as described previously (Hashizume & Sakata, 1989*b*) but the procedure was more complicated here because we had no direct access to the sample. We finely adjusted the sample height so that part of the collimated X-ray beam did not hit the sample surface but directly reached a photosensitive paper placed 1.5 m downstream *via* the Be

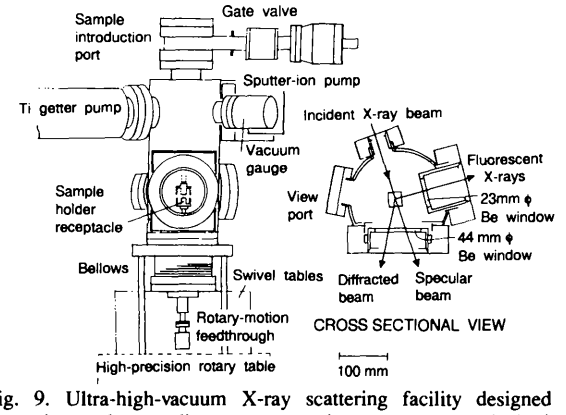

Fig. 9. Ultra-high-vacuum X-ray scattering facility designed for grazing-angle standing-wave experiments at a vertical-wiggler beamline of synchrotron radiation. The inset shows a cross-sectional view at the sample position, which is not to scale.

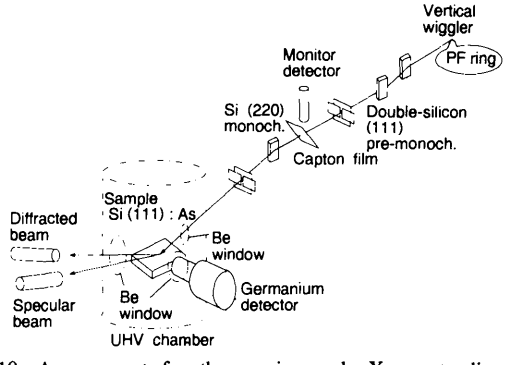

Fig. 10. Arrangement for the grazing-angle X-ray standing-wave experiment at the vertical-wiggler synchrotron source of the Photon Factory. The source–sample distance is $\sim$ 27 m. Half-slits in front of the specular-beam and diffracted-beam detectors are not shown. Also not shown is the high-precision rotary table mounting for the UHV chamber. The set-up downstream of the first slit is placed in a radiation safety hutch (not shown).

windows. This paper intercepted a specular-reflected beam from the sample as well, which served to evaluate the glancing-incidence angle by a measurement of the spacing of the two beam records. The specular beam and the Bragg-diffracted beam reached separate NaI detectors *via* a 44 mm-diameter beryllium window. A half-slit placed in front of the specular-beam detector blocked the direct beam, which set measured specular photon fluxes on a zero offset level. A similar blade was needed in front of the diffracted-beam detector: the beam penetrating into the sample and emerging from the lateral surface was quite strong. The photon flux of the specular beam was $10^6\ s^{-1}$. The sample emission was measured with an energy-dispersive high-purity germanium detector. The net X-ray fluorescence integrated over an energy range of the 10.5 keV As K line was of the order of 10 photons s^{-1}. The Photon Factory storage ring was injected with 2.5 GeV positrons to a stored current of 350 mA at the time of the experiment.

4. Results and discussion

Data points in Fig. 11 show specular reflected, Bragg diffracted and As fluorescence fluxes measured simultaneously as $\Delta\theta$ was scanned through the Si $\bar{2}20$ Bragg position ($\Delta\theta = 0$) for three fixed values of φ_0 near the critical angle for total external reflection, $\varphi_c = 1.85$ mrad. The specular and fluorescence fluxes are normalized with the use of the fluxes measured at θ 500 μrad off θ_B at the same φ_0 angles. The plots in Fig. 11 are not quite the same as published in the previous paper (Sakata, Hashizume & Kurashina, 1993). A post-experiment calibration, using an optical autocollimator, of the BL-14B high-precision rotary table, with the UHV facility mounted on it, yielded a conversion factor of 1.30(10)″/400 pulse-motor steps on the worm gear. Thus, the previous plots need to be multiplied by a factor 0.650 on the horizontal scale.* It was found later that the discrepancy between the default and real conversion factors was due to defects in the motor-control software but not to the load on the rotary table. We fitted the specular-intensity profiles to determine for each data set the φ_0 angle more accurately than estimated from the beam separation on the image detector. The fits showed $\varphi_0 = 1.12$ *vs* 1.11 mrad for (*a*), 1.86 *vs* 1.88 mrad for (*b*) and 2.64 *vs* 2.59 mrad for (*c*) (Table 1). The e.s.d. was smaller than 0.001 mrad in each fit. Thus, the beam-separation method evaluated the φ_0 angles within ±0.03 mrad errors. The diffraction profiles in Fig. 11 do not show the abrupt peak fall-off on the low-angle flanks caused by the evanescent diffracted beam (Cowan, 1985; Cowan, Brennan Jach, Bedzyk & Materlik, 1986; Sakata & Hashizume, 1988). This is accounted for by convolution effects.

* This does not affect the conclusion of the previous study (see later discussions).

The expression of the emission yield given in §2 includes three structure parameters for As atoms, x, f and Z. There is evidence (Bringans, 1992) supporting the model with As atoms substituting for the Si atoms at the topmost sites of the Si (111) double plane (Olmstead, Bringans, Uhrberg & Bachrach, 1986). An As atom is bonded to three second-layer silicon atoms in a symmetrical configuration, terminating the surface with a nonreactive lone-pair orbital. This indicates As atoms sitting on the ($\bar{2}20$) Bragg planes of the silicon crystal ($x = 0$). The Bragg planes, located at the peaks in the Fourier component of the electron-density distribution, coincide with the ($\bar{2}20$) atomic planes in the silicon crystal. As to the vertical height, a Bragg X-ray standing-wave study (Patel, Golovchenko, Freeland & Gossmann, 1987) indicates As atoms lying 0.96 Å above the unrelaxed top-layer Si atoms of the bulk-like (111)

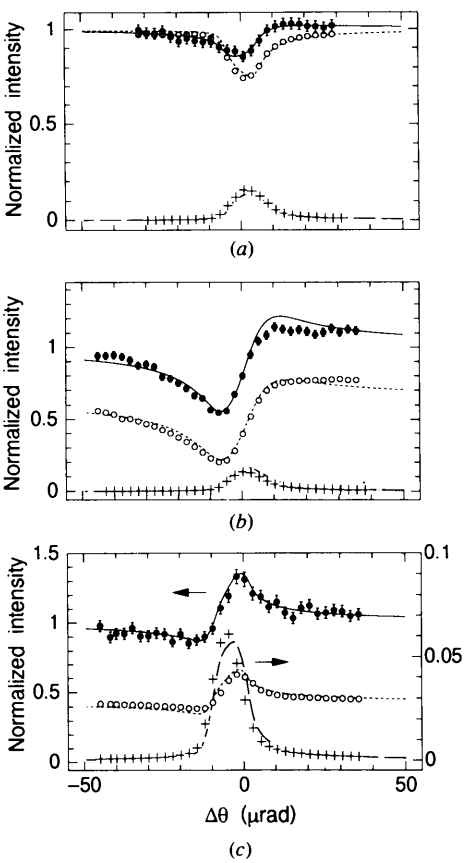

Fig. 11. As fluorescence signals (filled circles), specular-beam fluxes (open circles) and diffracted fluxes (crosses) observed from an Si (111):As 1 × 1 surface in grazing-angle diffraction for the Si ($\bar{2}20$) reflection in ultra-high vacuum at nominal glancing-incidence angles (*a*) $\varphi_0 = 1.11$ mrad, (*b*) 1.88 mrad and (*c*) 2.59 mrad. Error bars associated with the fluorescence data points indicate photon statistics. Lines are calculated using fitted φ_0 values (shown in Table 1) and take into account an instrument resolution function. For As atoms, parameters in Table 1 are assumed. Primary photon energy is 16.84 keV. The two bottom traces in (*c*) refer to the right ordinate.

Table 1. *Results of one-variable least-squares fits of the arsenic emission profiles observed from an* Si(111):As 1 × 1 *surface in grazing-angle diffraction*

X-ray glancing-incidence angles φ_0 were determined by fits of the simultaneously observed specular-reflection profiles. The fits of the emission data assume As atoms located 0.96 Å above the substrate silicon surface and on the Si ($\bar{2}20$) Bragg planes. The coherent fraction f for As atoms is the only fitting parameter. Numbers in parentheses are the e.s.d.'s in the least-significant digit.

φ_0 (mrad)	f	Weighted R factor
1.118*	0.90 (3)	0.016
1.863*	0.89 (2)	0.043
2.641*	0.81 (5)	0.029

* Associated e.s.d.'s are less than 0.001 mrad.

Table 2. *Results of two-variable least-squares fits of the arsenic emission profiles observed from an* Si(111):As 1 × 1 *surface in grazing-angle diffraction*

The fits assumed As atoms located 0.96 Å above the substrate silicon surface and varied the lattice position (x) and coherent fraction (f) parameters for each data set collected at the indicated X-ray glancing-incidence angle φ_0. Numbers in parentheses are the e.s.d.'s in the least-significant digit.

φ_0 (mrad)	x	f	Weighted R factor
1.118*	0.00 (1)	0.90 (2)	0.016
1.863*	0.00 (2)	0.89 (2)	0.043
2.641*	0.00 (3)	0.81 (5)	0.029

* Associated e.s.d.'s are less than 0.001 mrad.

surface. We thus used fixed parameters $x = 0$ and $Z = -0.96$ Å in our trial least-squares fits of the As emission data: f was the only variable parameter. Results of the fits, listed in Table 1, show that the three data sets, collected at different φ_0 angles, yielded very similar f values as they should. The lines in Fig. 11 show that the calculated emission profiles neatly fit the data (see also the R values in Table 1). All calculations take into account the in-surface divergence of the X-ray beam, $\delta\theta = 10.1$ μrad, owing to the monochromator, and the out-of-surface divergence $\Delta\varphi_0 = 0.20$ mrad, corresponding to the 4σ source size of the synchrotron beam and the limited flatness of the sample crystal.

Our second trial fits relaxed the x parameter in addition to f. The threefold symmetry of the Si (111) 1×1 surface indicates that if As atoms are off the ($\bar{2}20$) planes by x, positions 0 and $(1 - x)$ are also occupied by As atoms. Equal As occupancies are expected for the three positions for symmetry reasons. Our second fits thus assumed three equally occupied As sites. Results in Table 2 show, however, that the data do not support displaced As positions. It is notable that the As atoms are located on the ($\bar{2}20$) planes with a typical error of 2% in x. The obtained f values are very similar to those in Table 1 but they are not exactly the same. The close-to-unity f values indicate a highly ordered As structure.

Table 3. *Effects on the coherent fraction value (f) of the vertical height $-Z$ of* As *atoms assumed in the fits of the emission data*

All fits assume fraction f As atoms sitting on the Si ($\bar{2}20$) Bragg planes. Numbers in parentheses are the e.s.d.'s in the least-significant digit.

	$-Z$ (Å)		
φ_0 (mrad)	0.96	0.0	3.0
1.118	0.90 (3)	0.93 (3)	0.91 (3)
1.863	0.89 (2)	0.89 (2)	0.89 (2)
2.641	0.81 (5)	0.81 (5)	0.83 (5)

The theory of grazing-angle X-ray diffraction involves ambiguity about the location of the surface (Jach & Bedzyk, 1990). The surface is defined at the abrupt step in electron-density distribution but the exact position only affects the field damping factors. In our first trial fits of the As emission data, we placed the surface at the top Si (111) plane ($Z = -0.96$ Å). This surface is depicted as surface (I) in Fig. 12. Another possible choice is to locate the surface on the As plane, as shown by surface (II) in Fig. 12. In this case, $Z = 0$. Table 3 compares the results of least-squares fits assuming $Z = 0$ and $Z = -0.96$ Å with x fixed at 0 in both cases. No significant difference is seen in the f values determined by the two fits. Table 3 also shows the results of the fits assuming the As atoms at vertical height $Z = -3.0$ Å. The noncritical dependence of the f values on the vertical atom position is an important property of the grazing-angle X-ray standing-wave technique. No precise vertical information is needed for in-plane structure determinations. This is a consequence of the very slow variation of the external field intensity along the surface normal (Fig. 8). Fig. 13 shows this more clearly. Visible changes only occur in the field profile after a vertical displacement of ~ 5 Å. This is consistent with the field extension of ~ 50 Å above the surface in the range of incidence angles under discussion. We have to note, however, that f values determined from practical data are not completely independent of the Z values used in the analysis. This is also the case with x values. Grazing-angle X-ray standing waves above the surface have an intrinsic two-dimensional modulation, in contrast to the conventional Bragg standing waves.

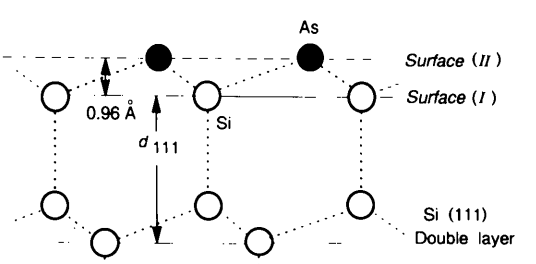

Fig. 12. Two definitions of the surface location for the Si(111):As 1 × 1 surface. As atoms occupy the threefold coordinated sites 0.96 Å above the top-layer (111) silicon plane.

The emission profiles in Fig. 11 are not similar to the bulk emission profiles observed from germanium crystals in grazing-angle diffraction. The latter signals show peaked profiles for $\varphi_0 < \varphi_c$, inclined steps with a high plateau on $\Delta\theta < 0$ and a low plateau on $\Delta\theta > 0$ for $\varphi_0 \simeq \varphi_c$ and dipped profiles for $\varphi_0 > \varphi_c$ (Cowan *et al.*, 1986; Hashizume & Sakata, 1989*a*,*b*; Jach & Bedzyk, 1993). This is explained by the penetration of the Bloch waves in the crystal (Jach, Cowan, Shen & Bedzyk, 1989). Like the Laue geometry in the absence of a specular reflection, Bloch wave 2 with nodes on the atomic planes is more penetrating than Bloch wave 1. For φ_0 less than φ_c, the field penetration is governed by the Fresnel extinction, and is as shallow as 30 Å for Bloch wave 1 and 60 Å for Bloch wave 2 at $\Delta\theta \simeq 0$ (Sakata & Hashizume, 1987). At off-Bragg angles, there is no Bloch wave generated and the field penetrates to a mean depth. X-ray emissions from the shallow layers are not appreciably absorbed before they reach the surface. The observed emission intensity will thus be proportional to the product of the field strength and the number of excited atoms, leading to a profile with a peak at $\Delta\theta \simeq 0$. For $\varphi_0 > \varphi_c$, on the other hand, the Fresnel extinction is unimportant and the true absorption dominates the field penetrations: X-ray fields penetrate as deep as 1 μm at off-Bragg conditions. The observed emission flux thus behaves as in the conventional Bragg geometry, where the Darwin-type extinction suppresses emissions at $\Delta\theta \simeq 0$ (Patel & Golovchenko, 1983).

5. Concluding remarks

The present work demonstrates for the first time that the grazing-angle X-ray standing wave can accurately determine the in-plane location and ordering of surface-adsorbed atoms in ultra-high vacuum. The high collimation and brilliance of synchrotron X-rays obtained from a wiggler source permitted the fluorescence to be monitored from As atoms present in a monolayer coverage on the Si(111) surface. Our grazing-angle X-ray standing-wave data indicate a highly ordered As structure on the Si(111):As 1×1 surface. As atoms occupy the high-symmetry sites coordinated by three Si atoms on a bulk-like Si(111) surface with little disorder. Displaced As positions are not supported by the observation. The same conclusion was reached in the previous paper (Sakata, Hashizume & Kurashina, 1993) by investigation of the characteristic dependence of the calculated emission profiles on the order and displacement parameters for X-ray glancing incidence angles smaller than φ_c. The least-squares analysis in the present study revealed that 80–90% of the As atoms actually occupy the high-symmetry sites. Our result would probably be consistent with the conclusion of ion-scattering experiments by Headrick & Graham (1988) and Copel, Tromp & Köhler (1988). Our data concern the fluorescence signal specific to As atoms and are more convincing.

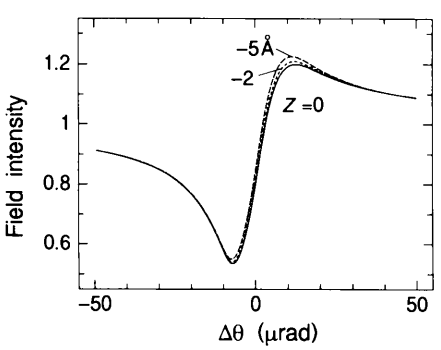

Fig. 13. Calculated field profiles at 0, 2 and 5 Å vertical heights above the surface ($Z = 0$). $\varphi_0 = 1.83$ mrad. Smeared by the experimental resolution function.

Conventional Bragg standing waves can also determine in-plane structures *via* triangulation of separate measurements performed with nonparallel reciprocal-lattice vectors. The grazing-angle technique using in-plane reciprocal-lattice vectors is more direct and provides a higher sensitivity and accuracy. We have demonstrated that the lattice positions of emissive atoms can be determined with errors of a few percent in a well ordered structure. The order parameter can be determined with an even higher accuracy from data collected in an appropriate range of glancing-incidence angle. The X-ray field localized in a shallow surface layer makes the geometry inherently sensitive to in-plane structures. Experiments are more difficult to perform, however, requiring control of the X-ray divergence and the sample orientation in the two orthogonal directions instead of just one.

The grazing-angle standing-wave technique will find interesting applications in thin films. The shallow field penetration does not require a bulk crystal to generate lattice-modulated standing waves. Our previous studies demonstrate that well developed dynamical standing waves are produced from crystals as thin as 100 Å (Sakata & Hashizume, 1991; Sakata, Kawamoto & Hashizume, 1992). Such fields would be useful in identifying the location of impurities at the surface and interface of heteroepitaxic layers.

We thank Professor F. Marumo for his interest in and support of our molecular-beam-epitaxy facility. We also appreciate assistance from H. Kurashina and I. Kawamoto. Discussions with Paul L. Cowan, who passed away immediately after the submission of this paper, were invaluable. We would like to dedicate the paper to him, as he pioneered the application of X-ray standing-wave techniques to surface-interface structures. The X-ray experiments described in this paper were supported by Photon Factory under proposals 88-085, 90-106 and 92-163. This work is supported by

Monbusho Grant-in-Aids for Scientific Research, nos. 03042052 and 06750025.

References

AFANASEV, A. M., IMAMOV, R. M., MASLOV, A. V. & MUKHAMEDZHANOV, E. KH. (1989). *Phys. Status Solidi A*, **113**, K153–K155.

AUTHIER, A. (1986). *Acta Cryst.* A**42**, 414–426.

BATTERMAN, B. W. & COLE, H. (1964). *Rev. Mod. Phys.* **36**, 681–717.

BRINGANS, R. D. (1992). *Crit. Rev. Solid State Mater. Sci.* **17**, 353–395.

COPEL, M., TROMP, R. M. & KÖHLER, U. K. (1988). *Phys. Rev. B*, **37**, 10756–10763.

COWAN, P. L. (1985). *Phys. Rev. B*, **32**, 5437–5439.

COWAN, P. L., BRENNAN, S., JACH, T., BEDZYK, M. J. & MATERLIK, G. (1986). *Phys. Rev. Lett.* **57**, 2399–2402

HASHIZUME, H. & SAKATA, O. (1989*a*). *J. Phys. (Paris) Colloq.* C7, *Suppl.* 10, **50**, 225–229.

HASHIZUME, H. & SAKATA, O. (1989*b*). *Rev. Sci. Instrum.* **60**, 2373–2375.

HEADRICK, R. L. & GRAHAM, W. R. (1988). *Phys. Rev. B*, **37**, 1051–1054.

ISHIZAKA, A. & SHIRAKI, Y. (1986). *J. Electrochem. Soc.* **133**, 666–671.

JACH, T. & BEDZYK, M. J. (1990). *Phys. Rev. B*, **42**, 5399–5402.

JACH, T. & BEDZYK, M. J. (1993). *Acta Cryst.* A**49**, 346–350.

JACH, T., COWAN, P. L., SHEN, Q. & BEDZYK, M. J. (1989). *Phys. Rev. B*, **39**, 5739–5747.

NAKAYAMA, K., TANAKA, M., ANNAKA, S., SUGII, K., TAKAHASHI, T., KIKUTA, S., ISHIKAWA, T., ANDO, M. & KOHRA, K. (1986). *X-ray Instrumentation for the Photon Factory: Dynamic Analysis of Microstructures in Matter*, edited by S. HOSOYA, Y. IITAKA & H. HASHIZUME, pp. 269–274. Tokyo: KTK Science.

OLMSTEAD, M. A., BRINGANS, R. D., UHRBERG, R. I. G. & BACHRACH, R. Z. (1986). *Phys. Rev. B*, **34**, 6041–6044.

PATEL, J. R. & GOLOVCHENKO, J. A. (1983). *Phys. Rev. Lett.* **50**, 1858–1861.

PATEL, J. R., GOLOVCHENKO, J. A., FREELAND, P. E. & GOSSMANN, H. J. (1987). *Phys. Rev. B*, **36**, 7715–7717.

ROBINSON, I. K. (1991). *Handbook on Synchrotron Radiation*, Vol. 3, edited by G. S. BROWN & D. E. MONCTON, pp. 221–266. Amsterdam: North-Holland.

SAITOH, Y., HASHIZUME, H. & TSUTSUI, K. (1988). *Jpn. J. Appl. Phys.* **27**, 1386–1396.

SAKATA, O. (1994). Thesis, Tokyo Institute of Technology, Japan.

SAKATA, O. & HASHIZUME, H. (1987). Rep. RLEMTIT, Vol. 12, pp. 45–57. Tokyo Institute of Technology, Japan.

SAKATA, O. & HASHIZUME, H. (1988). *Jpn. J. Appl. Phys.* **27**, L1976–L1979.

SAKATA, O. & HASHIZUME, H. (1991). Rep. RLEMTIT, Vol. 16, pp. 27–38. Tokyo Institute of Technology, Japan.

SAKATA, O. & HASHIZUME, H. (1995). *Rev. Sci. Instrum.* In the press.

SAKATA, O., HASHIZUME, H. & KURASHINA, H. (1993). *Phys. Rev. B*, **48**, 11408–11411.

SAKATA, O., KAWAMOTO, I. & HASHIZUME, H. (1992). Conference of the Asian Crystallographic Association, AsCA '92, 16Q-08, Singapore, 13–16 November 1992. Collected Abstracts.

Acta Cryst. (1995). A**51**, 384–390

Computing Accurate Bragg Diffraction Intensities by Simulation

BY E. RITTGER*

SBPM-DBCM-DSV, CEA-Centre d'Etudes Nucléaires de Saclay, F-91191 Gif sur Yvette CEDEX, France

(*Received* 5 *July* 1994; *accepted* 3 *January* 1995)

Abstract

The diffraction intensities obtained from a computer simulation of a crystal exhibit substantial finite-size effects and converge only very slowly to the thermodynamic limit when the simulation box is enlarged. Two procedures that improve the convergence by correcting for this effect are compared. One of them, the elasticity-tensor correction, is shown to yield highly accurate results with a small simulation box.

1. Introduction

The harmonic approximation of the Hamiltonian is a general and analytically convenient concept for studying the thermal and mechanical properties of crystalline substances at low temperature. It explains diffraction intensities in terms of averaged atomic positions and fluctuations and forms the basis for structure determination even when harmonicity is only a poor approximation. At high temperatures, however, when the system explores anharmonic regions of its phase space, it may not be good enough, especially if a system is to be studied in more detail than just a mean structure and temperature factors. Besides this, some crystals that contain liquids, *e.g.* protein crystals containing water, are not amenable to theories that allow atoms only to vibrate around mean positions. In such cases, computer simulation is nowadays the best tool. It is therefore desirable to have a general recipe for computing accurate theoretical diffraction intensities for a given potential-energy function by simulation.

Two theoretical concepts for such a recipe, the 'quasi-harmonic correction' and the 'elasticity-tensor correction' are presented in §§ 2 and 3. To test them, they are applied to a simple model described in § 4. The test results are shown and compared in §§ 5 and 6. § 7 gives a summary.

* Present address: Osnabruecker Strasse 22, D-10589 Berlin, Germany.